XRD AND TEM STUDIES ON NANOPHASE MANGANESE OXIDES IN FRESHWATER FERROMANGANESE NODULES FROM GREEN BAY, LAKE MICHIGAN

SEUNGYEOL LEE AND HUIFANG XU*

NASA Astrobiology Institute, Department of Geoscience, University of Wisconsin−Madison,
1215 West Dayton Street, A352 Weeks Hall, Madison, Wisconsin 53706

Abstract—Freshwater ferromanganese nodules (FFN) from Green Bay, Lake Michigan have been investigated by X-ray powder diffraction (XRD), micro X-ray fluorescence (XRF), scanning electron microscopy (SEM), high-resolution transmission electron microscopy (HRTEM), and scanning transmission electron microscopy (STEM). The samples can be divided into three types: Mn-rich nodules, Fe-Mn nodules, and Fe-rich nodules. The manganese-bearing phases are todorokite, birnessite, and buserite. The iron-bearing phases are feroxyhyte, goethite, 2-line ferrihydrite, and proto-goethite (intermediate phase between feroxyhyte and goethite). The XRD patterns from nodule cross sections suggest the transformation of birnessite to todorokite. The TEM-EDS spectra show that todorokite is associated with Ba, Co, Ni, and Zn; birnessite is associated with Ca and Na; and buserite is associated with Ca. The todorokite has an average chemical formula of $Ba^{2+}_{0.28}(Zn^{+2}_{0.14}Co^{3+}_{0.05}Ni^{2+}_{0.02})$ $(Mn^{4+}_{4.99}Mn^{3+}_{0.82}Fe^{3+}_{0.12}Co^{3+}_{0.05}Ni^{2+}_{0.02})\ O_{12}\cdot nH_2O$. Barium is the main cation in the structural tunnels of the todorokite. The average chemical formula of birnessite and Ca-buserite are: $Na^+_{0.14}Ca^{2+}_{0.19}(Mn^{4+}_{1.48}Mn^{3+}_{0.52})$ $O_4\cdot nH_2O$ and $Ca^{2+}_{0.27}(Mn^{4+}_{1.46}Mn^{3+}_{0.54})O_4\cdot nH_2O$, respectively. Most nodules have a concretionary structure of alternating Fe/Mn layers, commonly with a core of reddish feldspar containing phyllosilicates and hematite micro-crystals. Other cores consist of goethite, cristobalite, tridymite, hercynite, hematite-bearing quartz, coal, and chlorite-bearing rock fragments. The hexagonal or hexagonal-like structures of hematite micro-crystals and clay minerals in the cores may serve as heterogeneous nucleation sites for the Mn-oxides and Fe-(oxyhydr)oxides. The alternating Fe/Mn layers in FFNs might be caused by oscillatory redox condition fluctuations at the sediment-water interface due to changes in water level.

Key Words—Birnessite, Buserite, Ferromanganese Nodule, Green Bay, Heterogeneous Nucleation, HRTEM, Lake Michigan, Todorokite, XRD.

INTRODUCTION

Freshwater ferromanganese nodules (FFN) are known to occur in lakes throughout North America (Harriss and Troup, 1970; Callender *et al.*, 1973; Sozanski and Cronan, 1979; Stein *et al.*, 2001), Europe (Calvert and Price, 1970; Kuleshov and Sterenberg, 1988), Asia (Amirzhanov *et al.*, 1992; Tan *et al.*, 2006), and Africa (Williams and Owen, 1992; Kalindekafe, 1993). However, no detailed investigation has been reported about nano-phase minerals and nucleation of ferromanganese nodules in freshwater environments.

Green Bay FFN consist of alternating Fe/Mn layers around a central core, which undergo oscillatory changes between reduced and oxidized conditions at the sediment-water interface (Rossmann and Callender, 1968; Stein *et al.*, 2001; Hlawatsch *et al.*, 2002). Microbial communities are proposed to play a significant role in the mineralization of ferromanganese nodules (Nealson and Myers, 1992; Stein *et al.*, 2001). The Mn(II) and Fe(II) in the nodules are derived from igneous/metamorphic minerals

that constitute the bulk of glacial debris (Rossmann and Callender, 1968; Edgington and Callender, 1970). The glacial materials are quite permeable and thus easily weathered under temperate climatic conditions (Callender *et al.*, 1973; Robbins and Callender, 1975).

The purpose of the present paper is to offer further evidence of trace element binding behavior, nucleation sites, and growth of Green Bay nodules by using X-ray powder diffraction (XRD), scanning electron microscopy (SEM), high-resolution transmission electron microscopy (HRTEM), and scanning transmission electron microscopy (STEM). The Mineralogy of Green Bay nodules is todorokite, birnessite, buserite, feroxyhyte, goethite, ferrihydrite, and proto-goethite with a guyanaite structure (an intermediate phase between feroxyhyte and goethite) (Lee *et al.*, 2016). Given that the mineralogy of nanophase Fe-(oxyhydr)oxides in Green Bay nodules were strongly discussed in Lee *et al.*, (2016), the present paper will focus on the mineralogy of nanophase Mn-oxides, the transformation pathways between birnessite, buserite, and todorokite, and the associated trace elements Ba, Co, Ni, and Zn. Furthermore, a model to describe Fe/Mn-mineral nucleation on core minerals was proposed and the texture of alternating Fe/Mn layers in Green Bay nodules was described.

MATERIALS AND METHODS

Freshwater ferromanganese nodules

Ferromanganese nodules, which were previously studied by Callender *et al.*, (1973), were collected from the uppermost ~10 cm of lake-bottom sediments in Green Bay, Lake Michigan. The samples vary in diameter from ~0.5 to ~5 mm and can be divided into: Mn-rich nodules, Fe-Mn nodules, and Fe-rich nodules (Figures 1a, 1b, and 1c). Nodules from the northern area of Green Bay are primarily Fe-rich, whereas nodules adjacent to the Menominee River are Mn-rich (Callender *et al.*, 1973). Interestingly, the Fe/Mn ratios of FFNs increase from 0.7 in the central part of Green Bay to 10.8 in the north (Callender *et al.*, 1973).

Experimental methods

Multipoint Brunauer-Emmett-Teller (BET) surface areas and Barrett-Joyner-Halenda (BJH) pore size distributions were determined by N_2-adsorption techniques using a Nova 4200e surface area and pore size analyzer (Quantachrome instruments, Florida, USA) in the Geoscience Department at the University of Wisconsin-Madison. Surface area analyses of a reference material (Cat. No. 2005, Quantachrome instruments, Florida, USA; 108.1 ± 6.6 m^2/g) suggest that the measurement error was within $\pm 5\%$.

Two types of samples were prepared: one sample as polished thin sections (50 μm thickness) for *in situ* XRD; and the other sample was crushed and colloidal particles
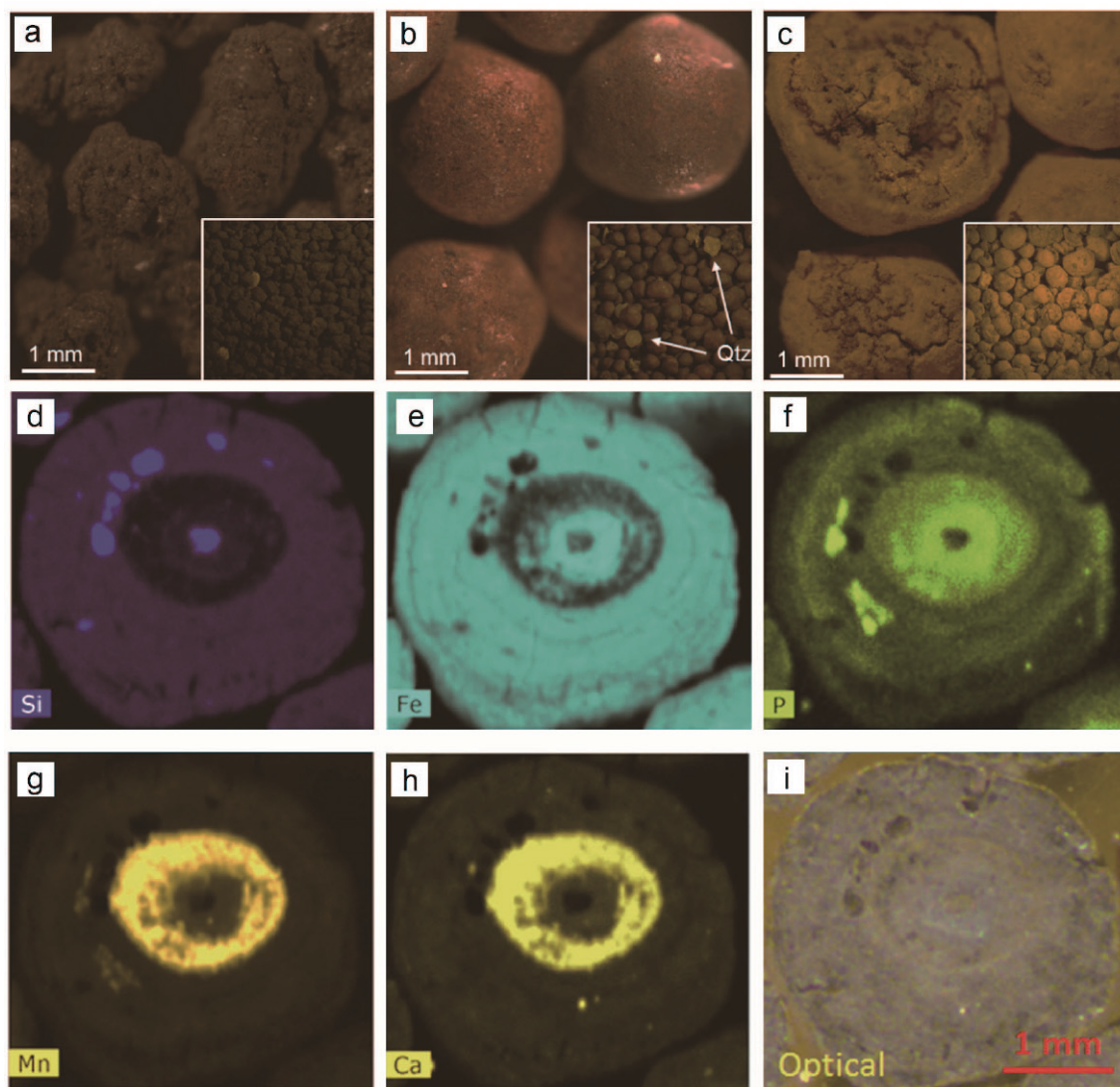

Figure 1. Optical images and element maps of Green Bay nodules: (a) Mn-rich nodules, (b) Fe-Mn nodules, (c) Fe-rich nodules, and (d−i) elemental maps and optical image of a nodule showing alternating Fe/Mn layers with an Fe-oxide-bearing quartz core.

were collected from a suspension to eliminate possible large detrital grains, such as quartz, for use in heating experiments. Mineral grains were also picked from cores in the nodules for XRD analyses. XRD data were collected on a 2-D image-plate detector using a Rigaku Rapid II instrument (Rigaku, Tokyo, Japan) using Mo-Kα radiation in the Geoscience Department. Two dimensional images were converted to produce conventional 2θ *vs.* intensity patterns using Rigaku's 2DP software. Percentages of mineral phases in the sample were calculated using the Rietveld method by using JADE 9 software (MDI, California, USA). A pseudo-Voigt method (Thompson *et al.*, 1987) was used for fitting the peak profiles.

Samples for SEM analysis were mounted onto glass slides, polished, and coated with carbon (~10 nm). All SEM images were obtained using a Hitachi S3400N variable pressure microscope (Hitachi, Tokyo, Japan) with an energy-dispersive X-ray attachment.

The elemental mappings of an Fe-Mn nodule cross section with a core (Fe-oxide-bearing quartz grain) was carried out using a Bruker M4 micro-XRF Imaging system (Bruker, Karlsruhe, Germany). The samples were analyzed using a Rh tube at 50 kV, 200 µA, and under 20 mbar vacuum. Two detectors were used to receive maximum counts. Elemental maps show that Si and P are associated with Fe (Figures 1d, 1e, and 1f) and Ca is generally associated with Mn (Figures 1g and 1h).

The HRTEM imaging and selected-area electron diffraction (SAED) analyses were performed using a Philips CM200-UT microscope (Philips, Eindhoven, Netherlands) operated at 200 kV equipped with a GE light-element energy-dispersive X-ray spectrometer (EDS) (Thermo Fisher Scientific, Pittsburgh, USA) at the Materials Science Center at the University of Wisconsin-Madison. Quantitative EDS results were obtained using experimentally determined k-factors from standards of silicate minerals (Hill, 2009). The STEM imaging was carried out at the Materials Science Center using an FEI Titan 80-200 (FEI, Oregon, USA), operated at 200 kV and equipped with an EDAX high-resolution EDS detector and a Gatan image filtering system (Gatan, California, USA). This instrument is capable of imaging single atoms with ~0.1 nm spatial resolution in STEM mode (Xu *et al.*, 2014). The STEM method uses a high-angle annular dark-field (HAADF) detector to support the most highly localized 1s Bloch state imaging (Pennycook *et al.*, 2000).

RESULTS

Surface area and pore size analysis

Green Bay nodules were studied through the BET surface area and BJH pore size distribution analyses to determine the nanopore structures of Mn-oxides and Fe-(oxyhydr)oxides. Multipoint BET surface areas of inner portions and the outer layer were 121 and 135 $m^2 g^{-1}$ for

the Mn-rich nodules, 120 and 132 $m^2 g^{-1}$ for Fe-Mn rich nodules, and 100 and 114 $m^2 g^{-1}$ for Fe-rich nodules, respectively. Similarly, BJH adsorption surface areas were 158 and 178 $m^2 g^{-1}$ for the Mn-rich nodules (inner part and outer layer), 144 and 165 $m^2 g^{-1}$ for the Fe-Mn nodules, and 115 and 124 $m^2 g^{-1}$ for the Fe-rich nodules (Figure 2). The increased Mn-oxide content was proportional to the increased surface area. In addition, the outer layers of FFN have slightly larger surface areas than the inner portion, consistent with the outer layers having more poorly crystallized minerals as young-stage precipitates. The BJH pore size distribution analyses show that the surface areas were dominated by nanopore surfaces (<10 nm) (Figure 2).

In situ XRD results

Diffraction data for selected regions of the thin section (Figure 3) showed that Mn-rich nodules were composed of todorokite, birnessite, buserite, quartz, and orthoclase.
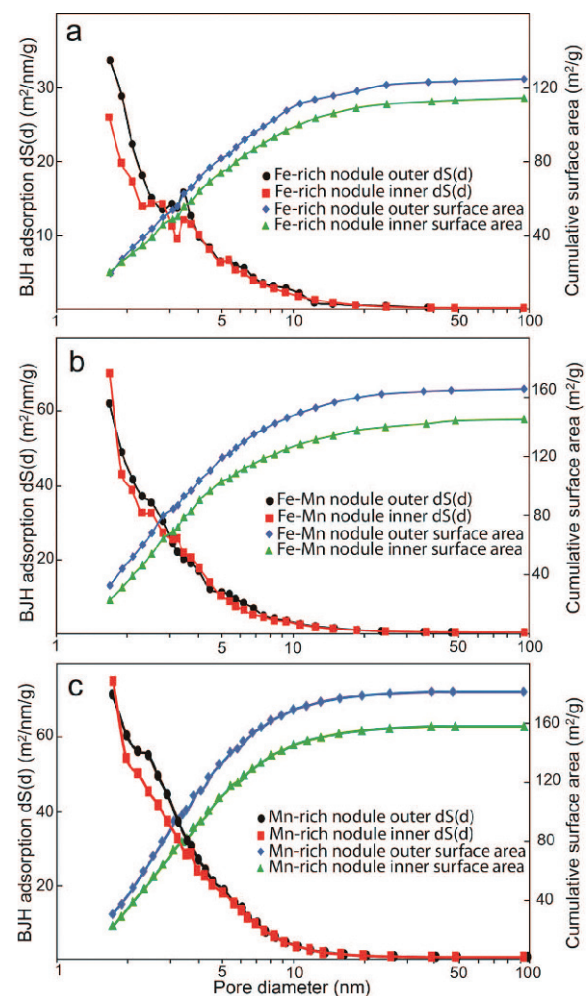

Figure 2. Diagrams illustrating BJH pore size distributions and cumulated surface areas for Green Bay FFN: (a) Mn-rich nodules, (b) Fe-Mn nodules, and (c) Fe-rich nodules. Pore size distribution (dS(d), m^2/nm/g) is the derivative of surface area as a function of pore diameter (d)
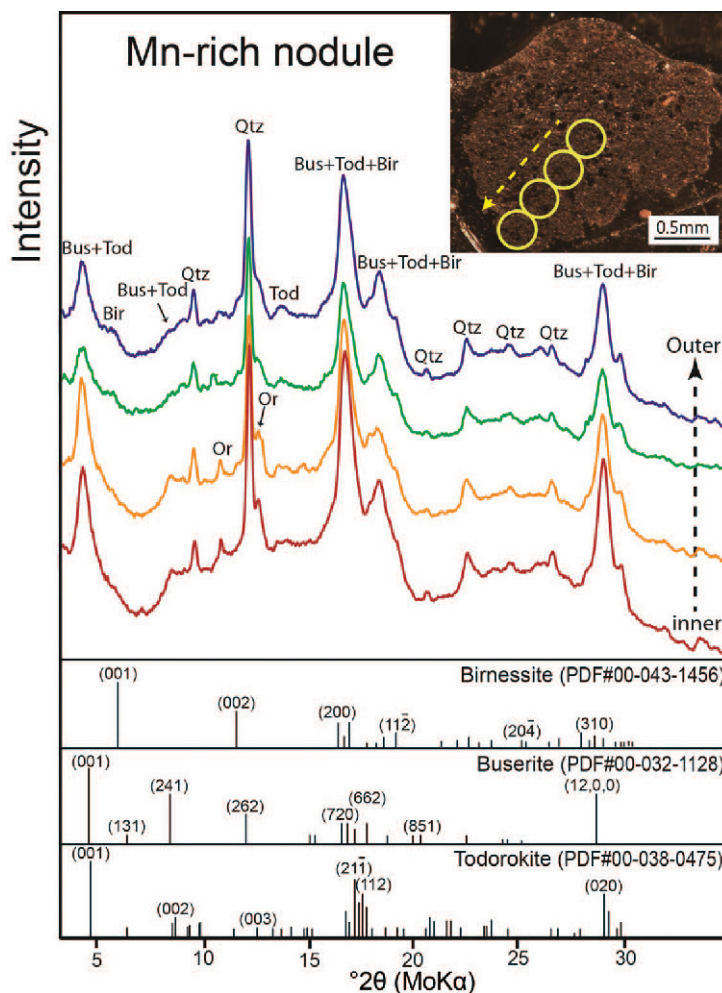
Figure 3. X-ray diffraction patterns of a Mn-rich nodule taken with 0.3 mm collimator. Yellow (white in grayscale) upper right circles are the XRD beam spots. Bus = buserite; Bir = birnessite; Tod = todorokite; Or = orthoclase; Q = quartz.

Mn-oxides are nanosized crystallites, as indicated by the broadness of the diffraction peaks (Figure 3). Todorokite is characterized by broad peaks at 9.63 Å (overlapped $(100)_{Tod}$ and $(001)_{Tod}$), 4.78 Å (overlapped $(200)_{Tod}$ and $(002)_{Tod}$), 3.00 Å $(301)_{Tod}$, 2.44 Å $(21\bar{1})_{Tod}$, and 1.41 Å $(020)_{Tod}$), whereas birnessite is characterized by peaks at 7.14 Å $(001)_{Bir}$, 3.58 Å $(002)_{Bir}$, 2.44 Å $(200)_{Bir}$, and 1.41 Å $(110)_{Bir}$ (Figure 3). The XRD peaks of buserite overlapped the todorokite pattern at 20°C; however, the buserite can be identified by the (001) peak spacing decrease to ~7 Å at 105°C due to loss of weakly bound interlayer H_2O in the interlayer positions (Figure 4) (Golden *et al.*, 1987). The 7.14 Å birnessite structure was almost destroyed at 200°C, whereas the 9.63 Å todorokite structure was stable to 400°C (Figure 4). The layer dimensions of Mn-octahedral sheets were increased due to the replacement of Mn^{2+} or Mn^{3+} in the Mn^{4+} site at 600°C (Figure 4). Mn-rich nodules transformed to braunite and iwakiite at 800°C (Figure 4). The results of Rietveld refinement showed the weight percentages of

transformed minerals: 50.7 wt.% braunite $(Mn_{0.8}Ca_{0.2})(Mn_{4.9}Fe_{1.1})O_8SiO_4$, 40.8 wt.% iwakiite $Mn(Fe_{1.2},Mn_{0.8})O_4$, 5.1 wt.% hematite (Fe_2O_3), and 3.4 wt.% ramsdellite (MnO_2) (Figure 4).

The nanophase Mn-oxides and Fe-(oxyhydr)oxides selectively interacted with certain core minerals in the FFN samples. Clean and pure quartz grains do not occur as core minerals of the Fe/Mn nanophase minerals (Figure 2). Figure 5 shows optical images and XRD patterns for the core minerals. Orthoclase, microcline, plagioclase, hematite-bearing quartz, goethite, cristobalite, hercynite, mullite, tridymite, amorphous SiO_2, coal, and rock fragments (containing hornblende, plagioclase, microcline, muscovite (*e.g.*, sericite), quartz, kaolinite, and chlorite) were identified (Figure 5). Reddish K-feldspar grains with hematite micro inclusions were the most common core minerals in Green Bay nodules (see Supplementary Table S1, deposited with the Editor-in-Chief and available at http://www.clays.org/JOURNAL/JournalDeposits.html). Both plagioclase and
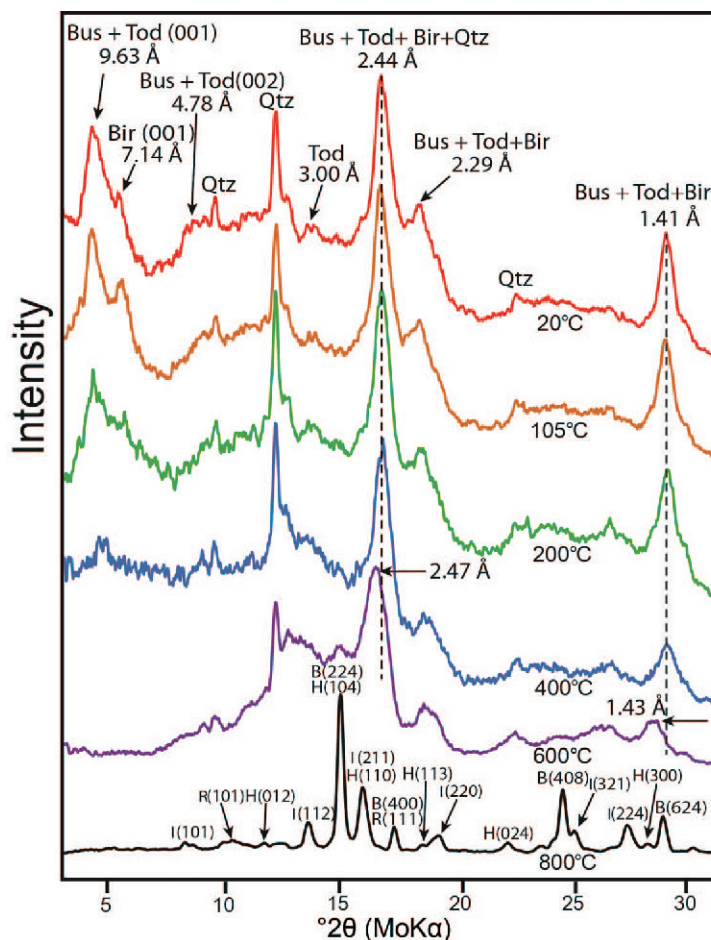
Figure 4. *In situ* X-ray diffraction patterns in heating experiments from 20 to 800°C. A Reitveld refinement of the 800°C XRD pattern is at bottom. Bus = buserite; Bir = birnessite; Tod = todorokite; Q = quartz; B = braunite; I = iwakiite; H = hematite; R = ramsdellite.

orthoclase grains contained a small amount of illite and kaolinite as weathering products. The high temperature minerals mullite, hercynite, and cristobalite with a vesicular texture (Figure 5) may be of anthropogenic origin.

SEM results

The SEM images of nodule cross-sections showed concretionary structures with alternating Fe/Mn layers (Figure 6). The thickness of the Fe/Mn layers varied from less than 10 to 200 μm (Figure 6). In back-scattered electron (BSE) images, Mn-oxides appeared brighter than Fe-(oxyhydr)oxides because todorokite contains Ba (Figures 6d and 6e). Alternating Fe/Mn outer layers from f1 to f3 (Figure 6e), EDS analyses revealed chemical variations in the Fe/Mn layers and indicated Si-P-Fe and Ba-Mn associations (Figures 6e and 6f). The Mn-oxides occurred as sponge-like spheres, whereas Fe-(oxyhydr)oxides formed rounded aggregates of nanoparticles (Figures 6g and 6h). Fe-(oxyhydr)oxides and Mn-oxides were precipitated or aggregated on the surface of core minerals (Figures 6i, 6j, and 6k). The hercynite has a

vesicular texture that contains cavities left by gas bubbles (Figure 6i). Figure 6j shows the texture of mullite plates and tridymite. The Fe-(oxyhydr)oxides were preferentially precipitated on the surface of tridymite instead of mullite (Figure 6j).

TEM results

The TEM images showed that birnessite and todorokite were the major phases in Mn-rich nodules (Figure 7). Bright-field TEM images revealed thin flakes of birnessite that have an SAED pattern with five diffraction rings at ~3.5, ~2.4, ~2.1, ~1.8, and ~1.4 Å (Figure 7a). A HRTEM image of birnessite showed a [001]-zone-axis octahedral sheet with (200), (110), and (020) lattice fringes that are evident in a fast Fourier transform (FFT) pattern (Figure 7b). A Z-contrast image of birnessite indicated ~7.2 Å lattice fringes and local expansion corresponding to the (001) *d* spacing with a thickness of ~4-5 nm (Figure 7c). In addition, the interlayer expansion (Figure 7c) suggests a continuous structure between buserite and birnessite. SAED patterns of fibrous aggregates of todorokite revealed d-spacings
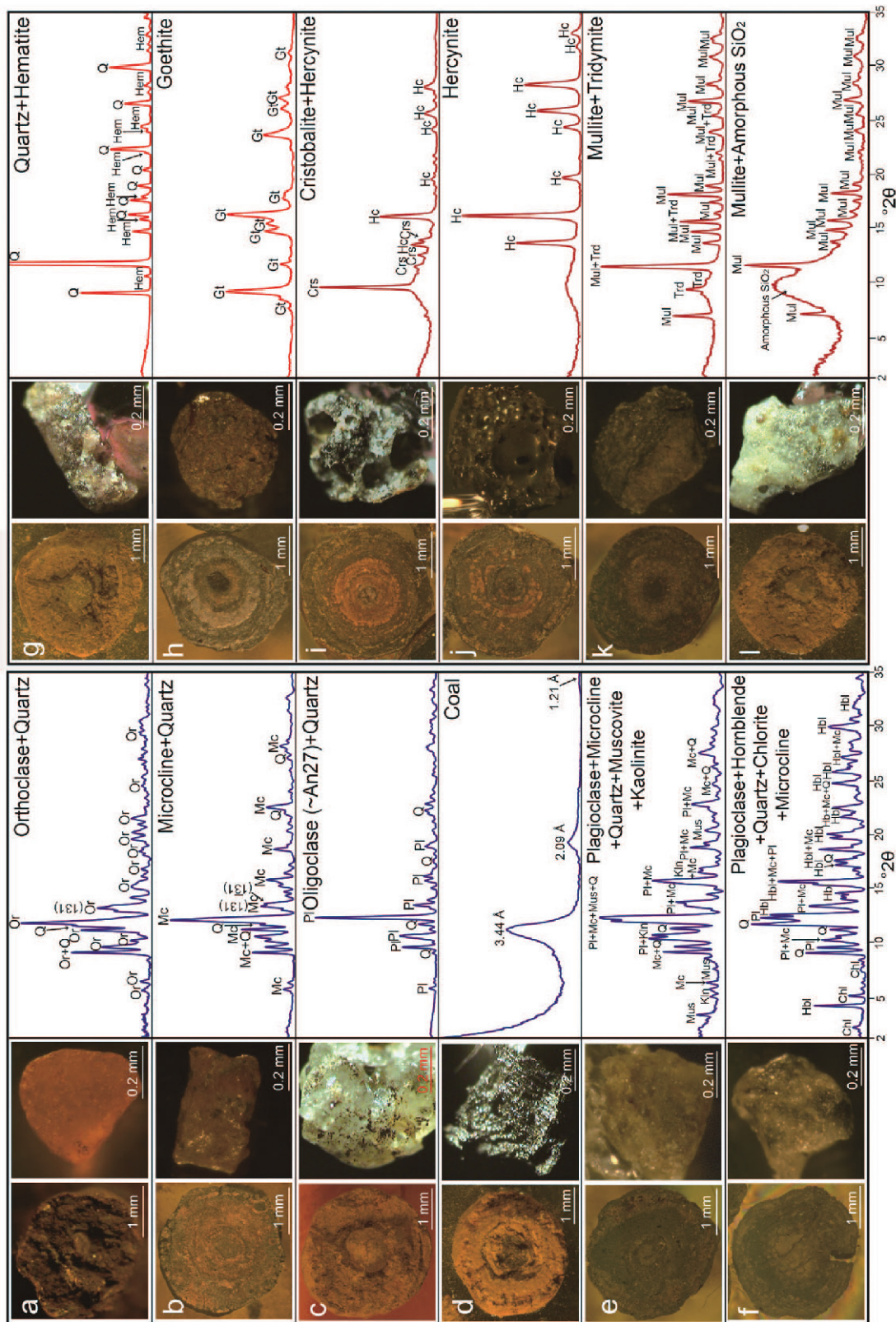
Figure 5. The optical images and XRD patterns of core minerals in the Green Bay FFN. Crs = cristobalite, Hc = hercynite, Mul = mullite, Trd = tridymite, Gt = goethite, Q = quartz, Hem = hematite, Mus = muscovite, Kln = kaolinite, Pl = plagioclase, Mc = microcline, Chl = chlorite, Hbl = hornblende, and Or =orthoclase. Details about the core minerals are listed in Table S1 (Supplementary Materials).
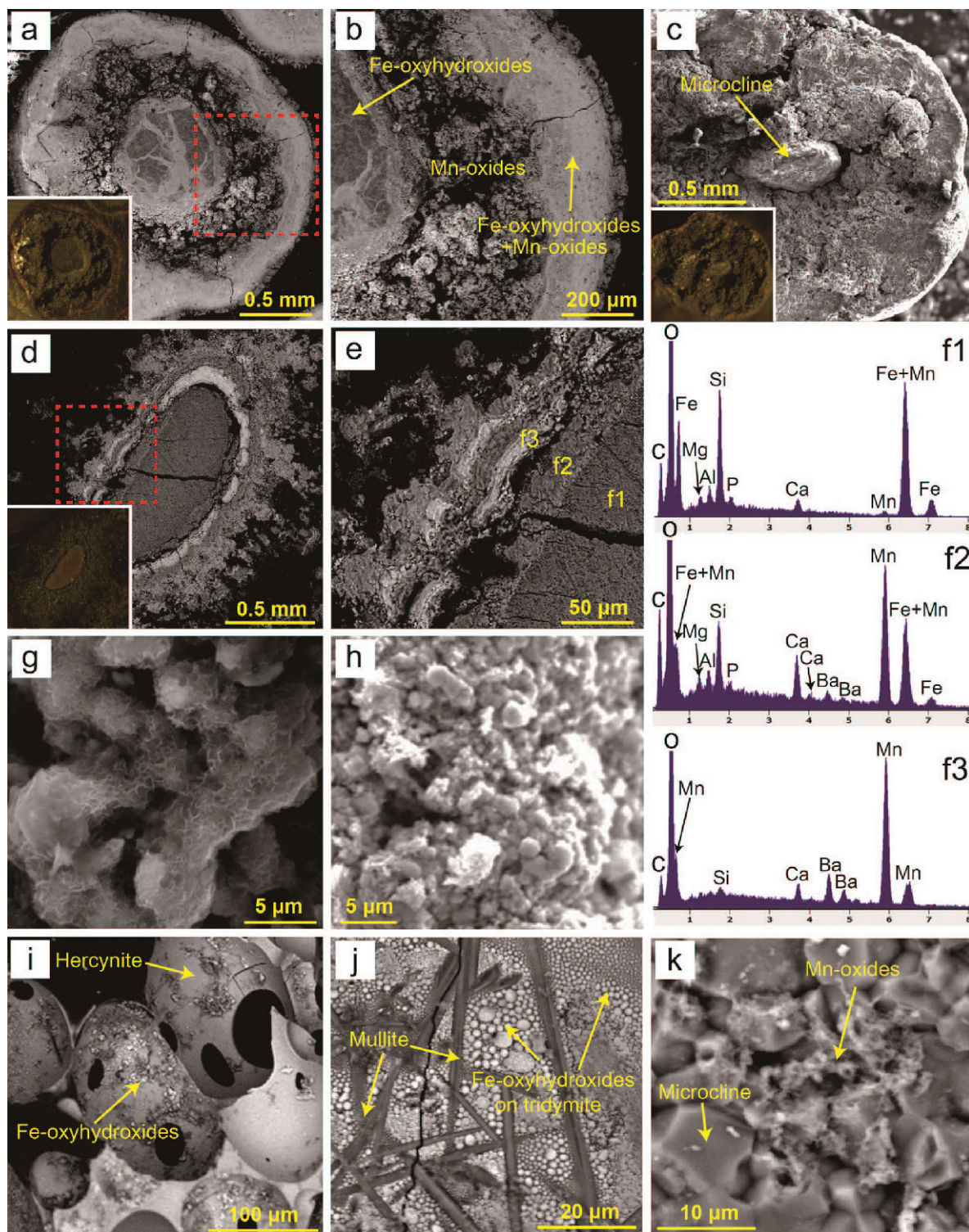
Figure 6. Optical image, BSE/SE images, and SEM-EDS showing Green Bay FFN cross sections: (a−c) Fe-rich nodule; (d−e) Mn-rich nodule; (f1−f3) SEM-EDS spectra from the layers of e; (g−h) high magnification images of Mn oxide and Fe oxyhydroxide; (i−k) core minerals.
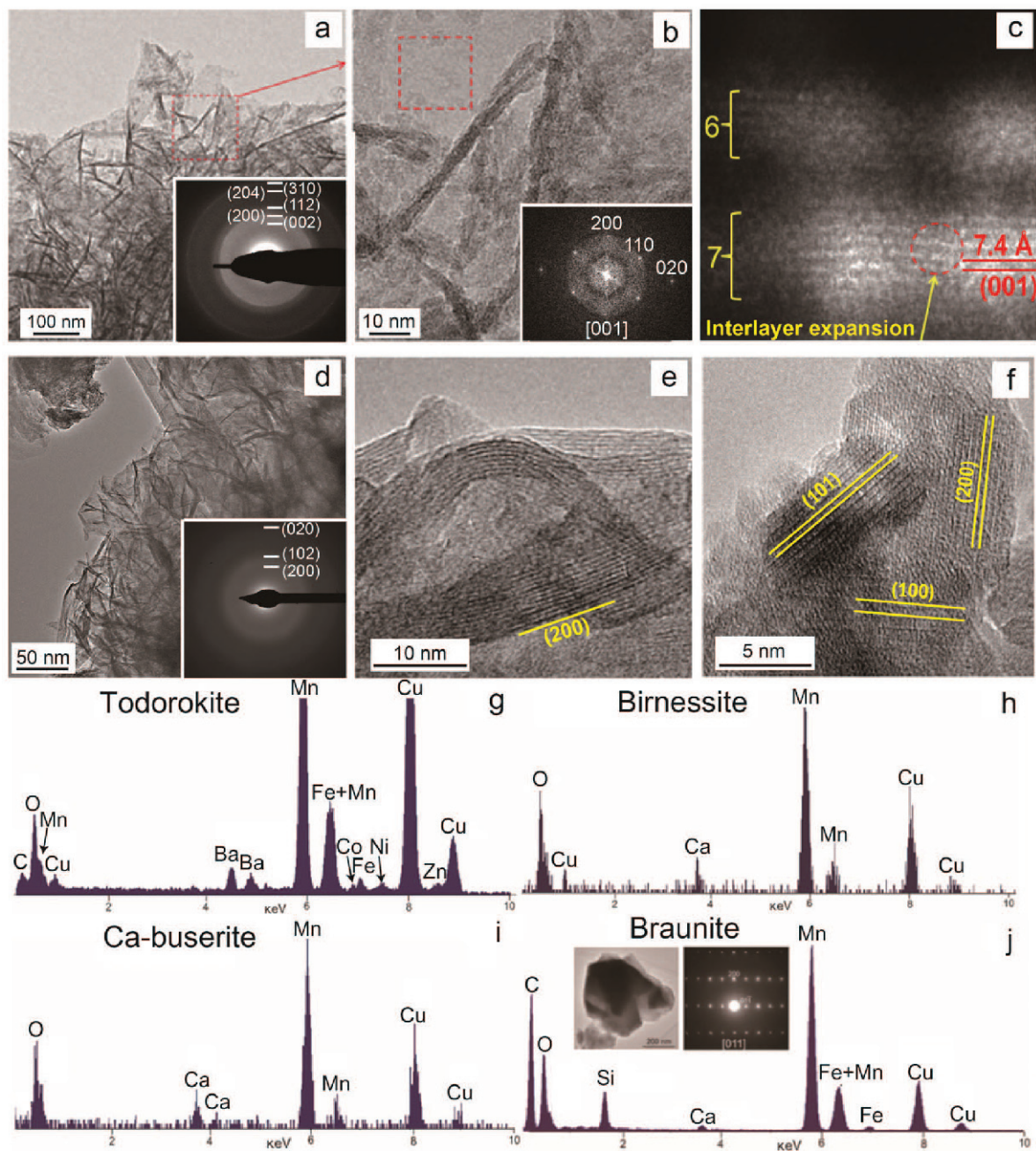
Figure 7. (a) Bright-field TEM image and SAED of birnessite; (b) HRTEM image of birnessite (dashed area, a) showing FFT patterns of the birnessite octahedral sheet; (c) Z-contrast image of birnessite showing interlayer expansion; (d) bright-field TEM image and SAED of the aggregated todorokite; (e) HRTEM image of fiber-like todorokite; (f) HRTEM image of well crystallized todorokite crystals; (g−i) X-ray EDS spectra of todorokite, birnessite, and Ca-buserite; (j) bright-field TEM image, SAED pattern, and X-ray EDS spectra of braunite. (a−c) are from Fe-Mn nodules (Figure 1b) and (d−i) are from Mn-rich nodules (Figure 1a).

corresponding to ~4.9, ~2.4, and ~1.4 Å (Figure 7d). The HRTEM images of todorokite showed (100) and (200) lattice fringes at 9.8 Å and 4.9 Å (Figures 7e and 7f). The d-spacings of both Mn-oxides correlate well with the XRD results (Figures 3 and 4) and are similar to the

dimensions reported in the literature (Post *et al.*, 2002; Marcus *et al.*, 2004; Manceau *et al.*, 2007; Barron and Torrent, 2013). The TEM-EDS spectra indicated that todorokite is associated with Ba, Co, Ni, and Zn (Figure 7g). Birnessite was associated with Na and Ca

(Figure 7h), whereas buserite was only associated with Ca (Figure 7i). The braunite identified in Mn-rich nodule heating experiments (Figure 1a) was confirmed by SAED patterns and EDS spectra (Figure 7j).

DISCUSSION

Mineralogy of nanophase manganese oxides

The main Mn-bearing phases in oxic sediments are todorokite, birnessite, and buserite (Burns, 1976). According to Dixon and White (2002), birnessite occurs in young soils and todorokite in young and intermediate-age soils. XRD data in the present study revealed similar relationships for the Mn-oxide distribution from birnessite to todorokite during freshwater ferromanganese nodule (FFN) formation (Figure 3). Birnessite occurred mainly in the outer layers of the samples, whereas the inner parts (*i.e.* old precipitates) contained more todorokite (Figure 3). This trend may indicate transformation from birnessite to todorokite (Golden *et al.*, 1987; Xu *et al.*, 2010)
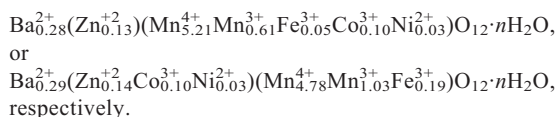
Mn-rich nodules mainly transformed to braunite, $(Mn_{0.8}Ca_{0.2})(Mn_{4.9}Fe_{1.1})O_8SiO_4$, and to iwakiite, $Mn(Fe_{1.2},Mn_{0.8})O_4$, at high temperature (800ºC) (Figure 4). Calculated bulk chemical compositions of the sample heated at 800ºC (Figure 4) are 59.5 wt.% ($MnO+Mn_2O_3+ Mn_2O$), 32.8 wt.% (Fe_2O_3), 6.5 wt.% (SiO_2), and 1.2 wt.% (CaO), and the Fe/Mn ratio and Ca composition was quite similar to previously reported values (Callender *et al.*, 1973). Metamorphosed banded manganese ore deposits from the Gozaisho mine in Japan and the Kalahari manganese field in South Africa were reported to contain braunite and iwakiite, which were associated with low-grade metamorphism and a sedimentary origin (Matsubara *et al.*, 1979; Gutzmer and Beukes, 2000). The primary source materials of both deposits may be similar to the Fe/Mn minerals of Green Bay FFN. Nano-phase Fe/Mn phases could transform to braunite and iwakiite during diagenesis and subsequent metamorphism.

Ba, Co, Ni, and Zn speciation of nanophase manganese oxides
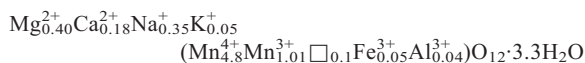
The nanophase Mn-oxides have large surface areas and high chemical activity, both of which contribute significantly to the adsorption of trace elements (Cornell and Schwertmann, 2003; Marcus *et al.*, 2004; Barron and Torrent, 2013). The trace element incorporation behavior of oceanic ferromanganese nodules is well known (Palumbo *et al.*, 2001; Marcus *et al.*, 2004; Manceau *et al.*, 2007; Manceau *et al.*, 2014). Previous studies revealed that Mn-oxides in marine nodules can incorporate Co, Cu, Ni, Pb, and Zn (Nowlan, 1976; Palumbo *et al.*, 2001; Koschinsky and Hein, 2003; Manceau *et al.*, 2007; Manceau *et al.*, 2014). Trace element incorporation in freshwater nodules have, however, received much less study (Stein *et al.*, 2001).

The TEM-EDS spectra indicated that the todorokite contains Ba, Co, Ni, and Zn (Figure 7g). In todorokite with a Mn 3×3 octahedral tunnel structure, Ba^{2+} is the main cation (Post, 1999; Xu *et al.*, 2010). The Co^{3+} and Ni^{2+} can be incorporated into Mn layer sites or be bonded to vacant sites, whereas Zn^{2+} is generally complexed at Mn octahedral sites by tridentate corner-sharing (Nowlan, 1976; Palumbo *et al.*, 2001; Koschinsky and Hein, 2003; Manceau *et al.*, 2007; Manceau *et al.*, 2014). The Fe^{3+} can substitute for Mn in octahedral layers due to the similar ionic size (Gutzmer and Beukes, 2000).
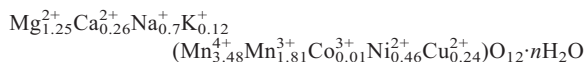
The Co^{3+} and Ni^{2+} are often found in natural todorokite samples (Post, 1999). The Co^{3+} and Ni^{2+} likely occur in the large Mn2 and Mn4 sites (Post, 1999). Depending on whether the Co^{3+} and Ni^{2+} are in the Mn sites or on nanocrystal surfaces, two chemical formulae for todorokite can be written as (Figure 7g):

$$Ba^{+2}_{0.28}(Zn^{+2}_{0.13})(Mn^{4+}_{5.21}Mn^{3+}_{0.61}Fe^{3+}_{0.05}Co^{3+}_{0.10}Ni^{2+}_{0.03})O_{12} \cdot nH_2O,$$
or
$$Ba^{+2}_{0.29}(Zn^{+2}_{0.14}Co^{3+}_{0.10}Ni^{2+}_{0.03})(Mn^{4+}_{4.78}Mn^{3+}_{1.03}Fe^{3+}_{0.19})O_{12} \cdot nH_2O,$$
respectively.

A chemical formula has been proposed for Ba-free todorokite from the Kalahari manganese ore (Gutzmer and Beukes, 2000):

$$Mg^{2+}_{0.40}Ca^{2+}_{0.18}Na^{+}_{0.35}K^{+}_{0.05}$$
$$(Mn^{4+}_{4.8}Mn^{3+}_{1.01}\square_{0.1}Fe^{3+}_{0.05}Al^{3+}_{0.04})O_{12} \cdot 3.3H_2O$$

Manceau *et al.*, (2014) proposed a formula of todorokite from oceanic nodules:

$$Mg^{2+}_{1.25}Ca^{2+}_{0.26}Na^{+}_{0.7}K^{+}_{0.12}$$
$$(Mn^{4+}_{3.48}Mn^{3+}_{1.81}Co^{3+}_{0.01}Ni^{2+}_{0.46}Cu^{2+}_{0.24})O_{12} \cdot nH_2O$$

The number of cations in tunnels or as adsorbed cations is related to the charge on the framework. The todorokite of Green Bay FFN has a similar Mn^{4+} content as the todorokite from the Kalahari manganese ores, whereas oceanic todorokite has a higher metal uptake capacity.

The TEM-EDS spectra indicated that buserite is associated with Ca, while birnessite is associated with both Na and Ca (Figures 7h and 7i). Birnessite from Green Bay FFN always contains Na and Ca together, but the Na:Ca ratio is variable. The average chemical formulae for the buserite $Ca^{2+}_{0.27}(Mn^{4+}_{1.46}Mn^{3+}_{0.54})O_4 \cdot nH_2O$ and birnessite $Na^{+}_{0.14}Ca^{2+}_{0.19}(Mn^{4+}_{1.48}Mn^{3+}_{0.52})O_4 \cdot nH_2O$ were calculated from X-ray EDS spectra, respectively. Most natural birnessite contains Ca (Ling *et al.*, 2015). The formula of synthetic Na-birnessite was reported as $Na^{+}_{0.58}(Mn^{4+}_{1.42}Mn^{3+}_{0.58})O_4 \cdot 1.5H_2O$ (Post *et al.*, 2002). In the chemical formula, Mn^{3+} is required to form buserite and birnessite (Post *et al.*, 2002). The Mn^{3+} in octahedral sites was proposed to be a major factor that causes the layers to deviate from hexagonal symmetry by the Jahn-Teller distortion (Drits *et al.*, 1997).

Transformation of birnessite and buserite to todorokite

The exact transformation from birnessite and buserite to todorokite has remained unclear due to the intermixed textures with poorly crystallized Mn-oxides (Golden *et al.*, 1987; Usui and Mita, 1995; Feng *et al.*, 2012). Atkins *et al.* (2014) presented a four-stage process for the transformation from birnessite to todorokite in marine diagenetic and hydrothermal environments. Pathway models were schematically proposed in the present study for the three Mn-oxide phases with associated trace elements based on TEM-EDS, XRD, heating experiments, and previously published studies (Figure 8). Todorokite is a tectomanganate structure consisting of triple chains of Mn-O octahedra that share corners to form tunnels, whereas birnessite and buserite have a layered phyllomanganate structure (Figure 8). Buserite interlayers contain a double layer of H_2O molecules together with divalent Ca^{2+} and Mg^{2+} cations, whereas birnessite interlayers contain a single layer of H_2O molecules together with Na^+ and K^+ (Golden *et al.*, 1987; Atkins *et al.*, 2014), although the cations can be replaced by other cations. Certain cations, such as Mg, Ca, and Ni, can expand the layers of birnessite to buserite (Golden *et al.*, 1987). Conversely, buserite with 10-Å layers can transform to a birnessite-like structure with a repeating 7-Å layer by losing weakly bound interlayer H_2O (Figures 4 and 8). Some buserite, however, which contains a high interlayer cation content, does not collapse to birnessite

(Novikov and Bogdanova, 2007). The XRD data from nodule cross sections support the transformation of birnessite to todorokite (Figure 3). Previous studies suggest that synthetic todorokite occurs by the transformation of phyllomanganate phases by way of either a refluxing process at atmospheric pressure or during hydrothermal treatment (Golden *et al.*, 1987; Shen *et al.*, 1993; Feng *et al.*, 2004; Cui *et al.*, 2009).

Nucleation of Green Bay FFN

The nucleation of Mn-oxides and Fe-(oxyhydr)oxides on mineral surfaces are important processes in natural aquatic systems. In general, Fe/Mn minerals nucleate on other mineral surfaces by heterogeneous nucleation (Rusch *et al.*, 2010; Hu *et al.*, 2013). Quartz coated with iron oxide has been reported to have much higher adsorption capabilities and reactive surface areas than pure quartz (Ying and Axe, 2005).

A nucleation model for the Green Bay FFN was proposed in the present study in which the hexagonally distributed oxygen atoms in core minerals (like phyllosilicates and hematite micro-crystal inclusions on feldspar surfaces and hematite associated with quartz) could serve as nucleation sites for nanophase Mn-oxides and Fe-(oxyhydr)oxides. Tridymite and graphite also show hexagonal structures on the (001) surfaces (Figure 9). Oxidized graphite or graphite-like (001) surfaces may have oxygen bound to the surface carbon (Figure 9). The Fe/Mn octahedra can combine with the surface oxygen
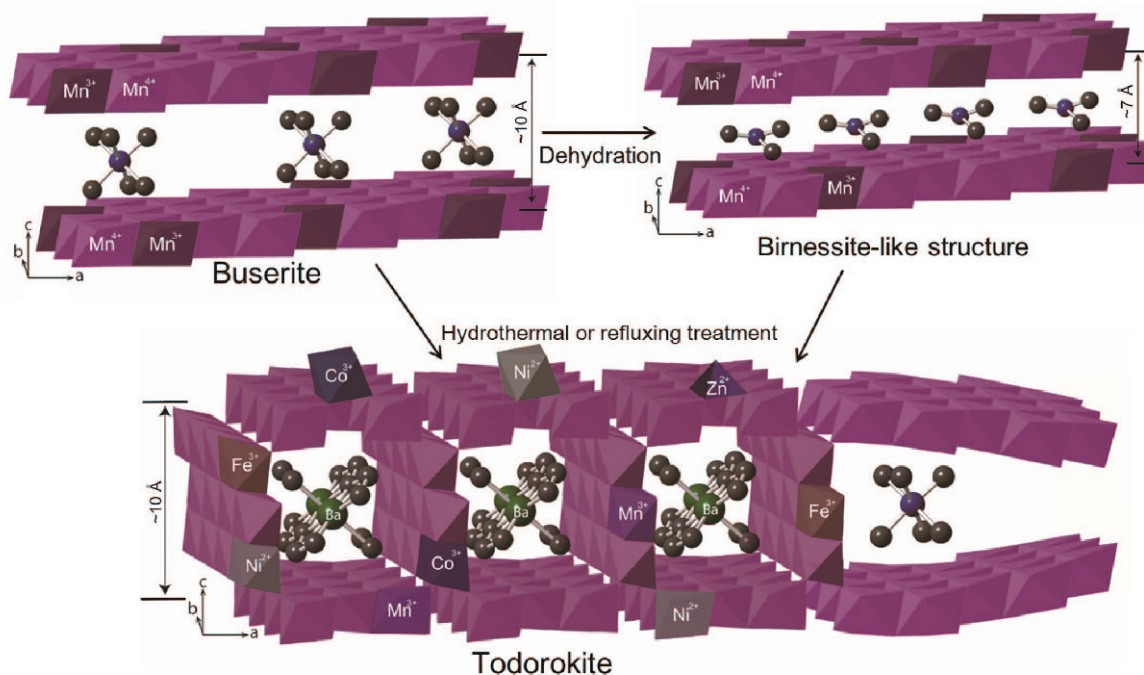

Figure 8. Schematic representation of structural models and transformation pathway from birnessite and buserite to todorokite (Golden *et al.*, 1987; Atkins *et al.*, 2014). Dark gray circles are water.
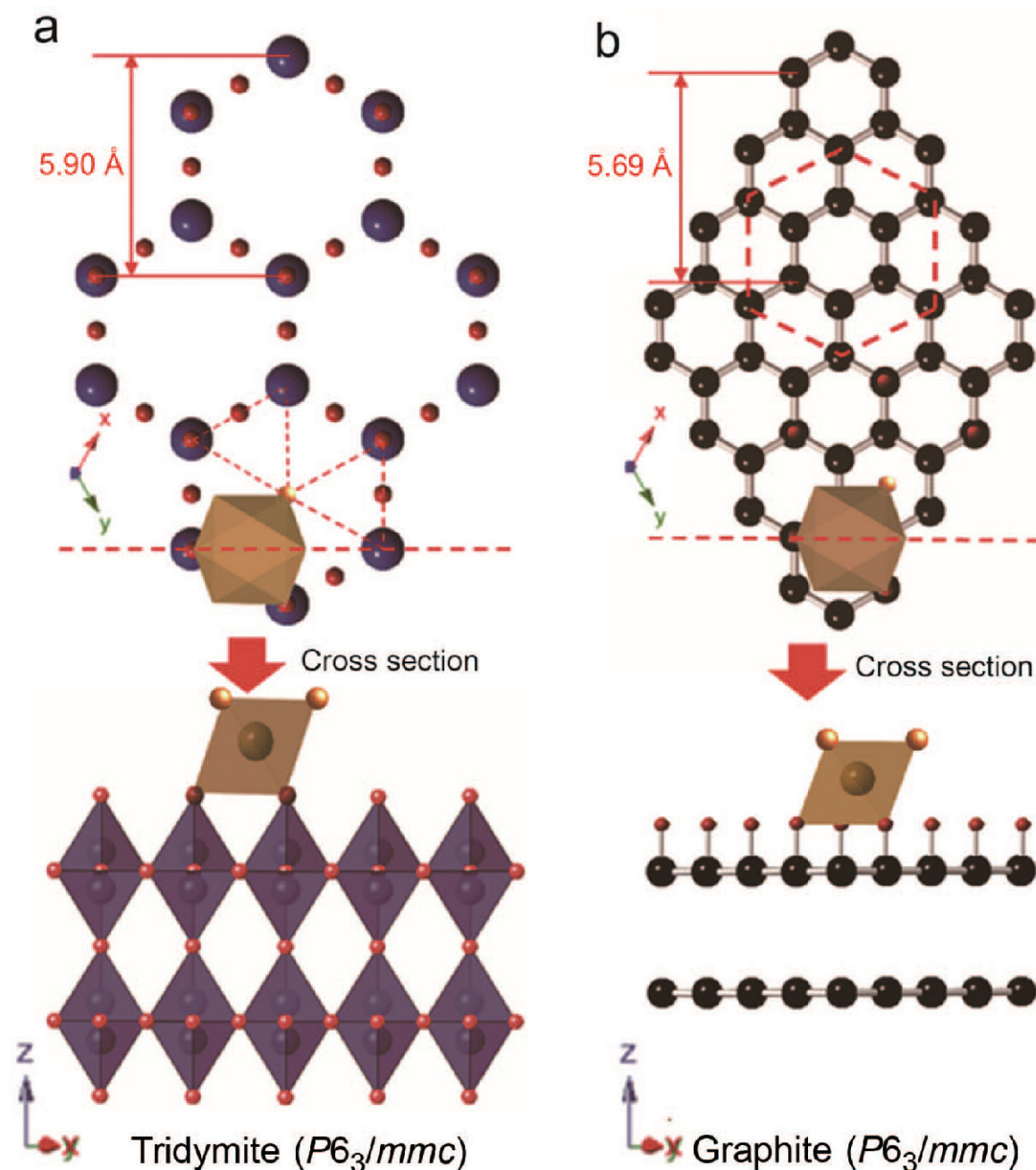
Figure 9. Ball-and-stick model of tridymite and oxidized graphite (for coal) showing hexagonal-like cation texture and cross sections.

atoms through slight surface distortions due to the hexagon-like packing of oxygen atoms on the (001) surfaces. Conversely, mullite and pure quartz do not serve as nucleation sites because no surfaces closely match Mn-O and Fe-O octahedra (Figure 6j).

Growth of alternating Fe/Mn layers of Green Bay FFN

Previous studies suggest that FFN were formed as a result of Fe and Mn oxidation in groundwater that is

discharging through porous sediments (Rossmann and Callender, 1968; Callender *et al.*, 1973). The Fe and Mn source for Green Bay FFN mainly includes Fe^{2+} and Mn^{2+} dissolution from lake sediments (glacial materials including chemically immature sediments) or the transport of groundwater enriched in Fe and Mn (Edgington and Callender, 1970; Callender *et al.*, 1973; Robbins and Callender, 1975). The redox cycling of Fe and Mn control the precipitation of Fe-(oxyhydr)oxides and Mn-

oxides around particles or by the formation of new layers on ferromanganese nodules (Hlawatsch *et al.*, 2002; Han *et al.*, 2003). The Fe-Mn oxidation may be mediated by microbial communities (Nealson and Myers, 1992; Stein *et al.*, 2001; Weber *et al.*, 2006; Shelobolina *et al.*, 2012).

Green Bay FFN have concretionary textures with alternating Fe/Mn layers (Figure 6). The BSE/EDS data show chemically oscillating trends among the Fe-rich layer, Fe/Mn-layer, and Mn-rich layer (Figures 6a−f). In order to explain the growth patterns as well as the distribution of Fe and Mn series, an Eh-pH diagram was drawn for the Fe–Mn–H_2O system showing Fe/Mn solubility and redox equilibria based on the geochemical conditions in previous studies (Callender *et al.*, 1973; Robbins and Callender, 1975) (Figure 10). The Eh-pH diagram in Figure 10 suggests that the stability field for amorphous Fe (to mimic poorly crystalline Fe-(oxy-hydr)oxides) is much greater than that for Mn phases or birnessite under the expected range of pH values. Iron can be separated from manganese by slow oxidation in the amorphous $Fe(OH)_3$ field before going to the birnessite field, whereas rapid oxidation could produce the mixed Fe/Mn layers (Figure 10). The chemical compositions of Fe/Mn layers are thus controlled by variations in the redox conditions.

The alternating layers in Green Bay FFN may have formed as a result of oscillatory changes in redox conditions at the water-sediment interface. Variations in redox conditions could be related to fluctuations in lake water levels (Figure 11). In addition, anthropogenic core

mineral phases (*e.g.* mullite and tridymite) suggest that nodules are young (growth rates: 1−3 mm/50 years = ~40 µm /year) (Figure 11). During lower water levels in Lake Michigan, Mn flux from sediments exceeded that of Fe due to increased oxygen concentrations at the sediment-water interface, leading to oxic conditions (Figures 10 and 11). Thus, Fe^{2+} is oxidized first even before reaching the sediment–water interface. The Mn^{2+} is oxidized at the interface because the Mn redox couple (Mn^{4+}/Mn^{2+}) has a higher redox potential than the Fe redox couple (Fe^{3+}/Fe^{2+}) (Figure 10). Conversely, during higher lake water levels, the Fe flux dominates due to increased anoxia at the water-sediment interface (Figures 10 and 11). The Mn-rich layers were thus deposited in a season with lower water levels, whereas the Fe-rich layers formed during higher water levels (Figure 11). Similarly, Fe-rich nodules from the northern area of Green Bay occur at greater water depths than Mn-rich nodules (Callender *et al.*, 1973).

CONCLUSIONS

Combined *in situ* XRD and TEM and associated techniques are very useful to identify nanophase minerals and measure the chemical compositions. Previous studies only showed correlations between Fe/Mn ratios and trace elements. The methods used here, however, can provide the detailed chemical compositions of individual nanophase manganese oxides and associated trace elements. These methods can be applied to understand speciation of heavy metals and trace
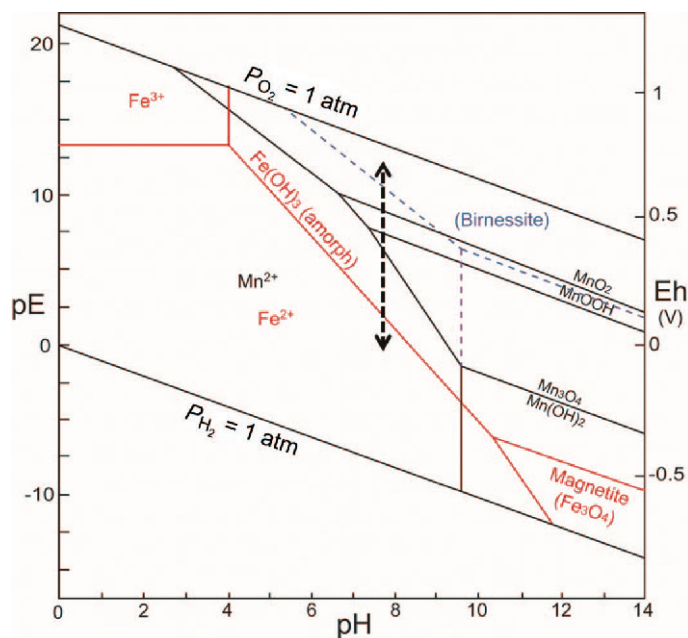

Figure 10. Eh-pH diagram for the Fe−Mn−H_2O system for Green Bay FFN ($\alpha_{Mn}= 10^{-4}$ M, $\alpha_{Fe}= 10^{-4}$ M, 1atm, and $T = 25$ºC). Thermodynamic data are from Callender *et al.* (1973). Based on its Mn^{4+}/Mn^{3+} ratio, the boundary for birnessite (dashed lines) is qualitatively placed under suppressed MnOOH and Mn_3O_4 conditions.
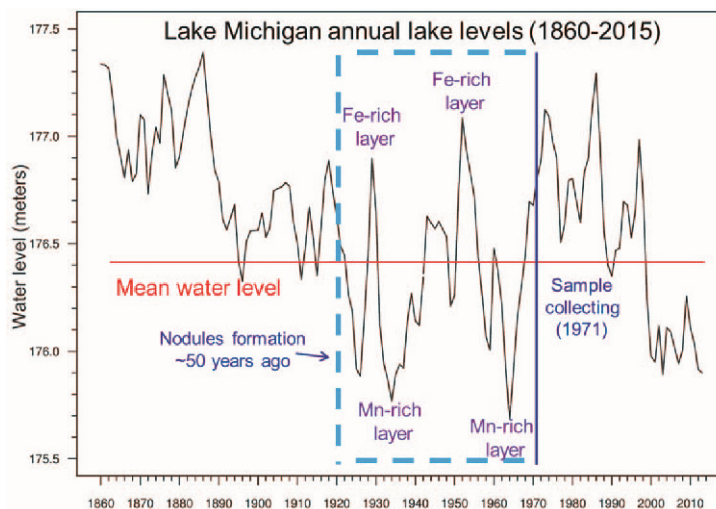
Figure 11. Water levels on Lake Michigan from 1860 to 2015. Data is from http://www.glerl.noaa.gov/data/now/wlevels/lowlevels/plot/MichHuron.jpg. The red (gray) line is the mean lake water level. Samples were collected in 1971. Anthropogenic core mineral phases (*e.g.* mullite and vesicular cristobalite) suggest that nodules are young (~50 years ago). Fe-rich layers are formed during the higher water level season, while Mn-rich layers are deposited during the lower water level season.

elements in nano-phase minerals in aquatic environments.

Presented here was a heterogeneous nucleation process for freshwater ferromanganese nodules. The nucleation sites for Green Bay FFN were associated with the hexagonal or hexagonal-like structures on mineral surfaces (hematite micro-crystals, clay minerals, oxidized graphite, and tridymite). That is why clean and pure quartz grains do not occur as core minerals in the Green Bay Fe/Mn nodules. The results may also contribute to a better understanding of the growth and formation of Fe-(oxyhydr)oxide concretions in sediments and sandstones.

REFERENCES

Amirzhanov, A.A., Pampura, V.D., Piskunova, L.F., and Karabanov, E.B. (1992) Geochemical types of ferromanganese nodules of Lake Baikal. *Russian Academy of Sciences*, **326**, 530−534.

Atkins, A.L., Shaw, S., and Peacock, C.L. (2014) Nucleation and growth of todorokite from birnessite: Implications for trace-metal cycling in marine sediments. *Geochimica et Cosmochimica Acta*, **144**, 109−125.

Barron, V. and Torrent, J. (2013) Iron, manganese and aluminium oxides and oxyhydroxides. *Minerals at the Nanoscale*, **14**, 297−336.

Burns, R.G. (1976) Uptake of cobalt into ferromanganese nodules, soils, and synthetic manganese(IV) oxides. *Geochimica et Cosmochimica Acta*, **40**, 95−102.

Callender, E., Bowser, C.J., and Rossmann, R. (1973) Geochemistry of ferromanganese and manganese carbonate crusts from Green Bay, Lake-Michigan. *Transactions-American Geophysical Union*, **54**, 340.

Calvert, S.E. and Price, N.B. (1970) Composition of manganese nodules and manganese carbonates from Loch Fyne, Scotland. *Contributions to Mineralogy and Petrology*, **29**, 215−233.

Cornell, R.M. and Schwertmann, U. (2003) *The Iron Oxides: Structure, Properties, Reactions, Occurrences, and Uses*. 2nd, completely revised and extended edition, 664 p. Wiley-VCH, Weinheim.

Cui, H.J., Feng, X.H., Tan, W.F., He, J.Z., Hu, R.G., and Liu, F. (2009) Synthesis of todorokite-type manganese oxide from Cu-buserite by controlling the pH at atmospheric pressure. *Microporous and Mesoporous Materials*, **117**, 41−47.

Dixon, J.B and White, G.N. (2002) Manganese oxides. Pp. 367−388 in: *Soil Mineralogy with Environmental Applications* (J.B. Dixon and D.G. Schulze, editors). Soil Science Society of America Book series **7**. Madison, Wisconsin.

Drits, V.A., Silvester, E., Gorshkov, A.I., and Manceau, A. (1997) Structure of synthetic monoclinic Na-rich birnessite and hexagonal birnessite: 1. Results from X-ray diffraction and selected-area electron diffraction. *American Mineralogist*, **82**, 946−961.

Edgington, D. and Callender, E. (1970) Minor element geochemistry of Lake Michigan ferromanganese nodules. *Earth and Planetary Science Letters*, **8**, 97−100.

Feng, J.L., Lin, Y.C., Gao, S.P., and Zhang, J.F. (2012) Enrichment of trace elements in ferromanganese concretions from terra rossa and their potential desorption. *Geochemical Journal*, **46**, 151−161.

Feng, X.H., Tan, W.F., Liu, F., Wang, J.B., and Ruan, H.D. (2004) Synthesis of todorokite at atmospheric pressure. *Chemistry of Materials*, **16**, 4330−4336.

Golden, D.C., Chen, C.C., and Dixon, J.B. (1987) Transformation of birnessite to buserite, todorokite, and

manganite under mild hydrothermal treatment. *Clays and Clay Minerals*, **35**, 271−280.

Gutzmer, J. and Beukes, N.J. (2000) Asbestiform manjiroite and todorokite from the Kalahari manganese field, South Africa. *South African Journal of Geology*, **103**, 163−174.

Han, X.Q., Jin, X.L., Yang, S.F., Fietzke, J., and Eisenhauer, A. (2003) Rhythmic growth of Pacific ferromanganese nodules and their Milankovitch climatic origin. *Earth and Planetary Science Letters*, **211**, 143−157.

Harriss, R.C. and Troup, A.G. (1970) Chemistry and origin of freshwater ferromanganese concretions. *Limnology and Oceanography*, **15**, 702−712.

Hill, T.R. (2009) High-resolution transmission electron microscopy investigation of nano-crystals of pyroxene and copper in oregon sunstones. Master thesis, University of Wisconsin-Madison, Wisconsin, USA.

Hlawatsch, S., Neumann, T., van den Berg, C.M.G., Kersten, M., Harff, J., and Suess, E. (2002) Fast-growing, shallow-water ferro-manganese nodules from the western Baltic Sea: origin and modes of trace element incorporation. *Marine Geology*, **182**, 373−387.

Hu, Y.D., Neil, C., Lee, B., and Jun, Y.S. (2013) Control of heterogeneous Fe(III) (hydr)oxide nucleation and growth by interfacial energies and local saturations. *Environmental Science & Technology*, **47**, 9198−9206.

Kalindekafe, L.S.N. (1993) The mineralogy of Lake Malawi ferromanganese nodules. *Journal of African Earth Sciences*, **17**, 183−192.

Koschinsky, A. and Hein, J.R. (2003) Uptake of elements from seawater by ferromanganese crusts: Solid-phase associations and seawater speciation. *Marine Geology*, **198**, 331−351.

Kuleshov, B.N. and Sterenberg, L.E. (1988) Isotopic composition of Fe-Mn-concretions of Lake Krasnoe. *International Geology Review*, 1092−1103.

Lee, S., Shen, Z., and Xu, H. (2016) Study on nanophase iron oxyhydroxides in freshwater ferromanganese nodules from Green Bay, Lake Michigan, with implications for the adsorption of As and heavy metals. *American Mineralogist*, **101**, 1986−1995.

Manceau, A., Kersten, M., Marcus, M.A., Geoffroy, N., and Granina, L. (2007) Ba and Ni speciation in a nodule of binary Mn oxide phase composition from Lake Baikal. *Geochimica et Cosmochimica Acta*, **71**, 1967−1981.

Manceau, A., Lanson, M., and Takahashi, Y. (2014) Mineralogy and crystal chemistry of Mn, Fe, Co, Ni, and Cu in a deep-sea Pacific polymetallic nodule. *American Mineralogist*, **99**, 2068−2083.

Marcus, M.A., Manceau, A., and Kersten, M. (2004) Mn, Fe, Zn and As speciation in a fast-growing ferromanganese marine nodule. *Geochimica et Cosmochimica Acta*, **68**, 3125−3136.

Matsubara, S., Kato, A., and Nagashima, K. (1979) Iwakiite, $Mn^{2+}(Fe^{3+}, Mn^{3+})_2O_4$, a new tetragonal spinelloid mineral from the Gozaisho mine, Fukushima Prefecture, Japan. *Mineralogical Journal*, **9**, 383−391.

Nealson, K.H. and Myers, C.R. (1992) Microbial reduction of manganese and iron – new approaches to carbon cycling. *Applied and Environmental Microbiology*, **58**, 439−443.

Novikov, G.V. and Bogdanova, O.Y. (2007) Transformations of ore minerals in genetically different oceanic ferromanganese rocks. *Lithology and Mineral Resources*, **42**, 303−317.

Nowlan, G.A. (1976) Concretionary manganese-iron oxides in streams and their usefulness as a sample medium for geochemical prospecting. *Journal of Geochemical Exploration*, **6**, 193−210.

Palumbo, B., Bellanca, A., Neri, R., and Roe, M.J. (2001) Trace metal partitioning in Fe-Mn nodules from Sicilian soils, Italy. *Chemical Geology*, **173**, 257−269.

Pennycook, S.J., Rafferty, B., and Nellist, P.D. (2000) Z-contrast imaging in an aberration-corrected scanning transmission electron microscope. *Microscopy and Microanalysis*, **6**, 343−352.

Post, J.E. (1999) Manganese oxide minerals: Crystal structures and economic and environmental significance. *Proceedings of the National Academy of Sciences of the United States of America*, **96**, 3447−3454.

Post, J.E., Heaney, P.J., and Hanson, J. (2002) Rietveld refinement of a triclinic structure for synthetic Na-birnessite using synchrotron powder diffraction data. *Powder Diffraction*, **17**, 218−221.

Robbins, J.A. and Callender, E. (1975) Diagenesis of manganese in Lake-Michigan sediments. *American Journal of Science*, **275**, 512−533.

Rossmann, R. and Callender, E. (1968) Manganese nodules in Lake Michigan. *Science*, **162**, 1123−1124.

Rusch, B., Hanna, K., and Humbert, B. (2010) Coating of quartz silica with iron oxides: Characterization and surface reactivity of iron coating phases. *Colloids and Surfaces a-Physicochemical and Engineering Aspects*, **353**, 172−180.

Shelobolina, E.S., Xu, H., Konishi, H., Kukkadapu, R., Wu, T., Blöthe, M., and Roden, E.E. (2012) Microbial lithotrophic oxidation of structural Fe(II) in biotite. *Applied and Environmental Microbiology*, **78**, 5746−5752.

Shen, Y.F., Zerger, R.P., Deguzman, R.N., Suib, S.L., Mccurdy, L., Potter, D.I., and Oyoung, C.L. (1993) Manganese oxide octahedral molecular sieves: preparation, characterization, and applications. *Science*, **260**, 511−515.

Sozanski, A.G. and Cronan, D.S. (1979) Ferromanganese concretions in Shebandowan Lakes, Ontario. *Canadian Journal of Earth Sciences*, **16**, 126−140.

Stein, L.Y., La Duc, M.T., Grundl, T.J., and Nealson, K.H. (2001) Bacterial and archaeal populations associated with freshwater ferromanganous micronodules and sediments. *Environmental Microbiology*, **3**, 10−18.

Tan, W.F., Liu, F., Li, Y.H., Hu, H.Q., and Huang, Q.Y. (2006) Elemental composition and geochemical characteristics of iron-manganese nodules in main soils of China. *Pedosphere*, **16**, 72−81.

Usui, A. and Mita, N. (1995) Geochemistry and mineralogy of a modern buserite deposit from a hot-spring in Hokkaido, Japan. *Clays and Clay Minerals*, **43**, 116−127.

Weber, K.A., Urrutia, M.M., Churchill, P.F., Kukkadapu, R.K, and Roden, E.E. (2006) Anaerobic redox cycling of iron by freshwater sediment microorganisms. *Environmental Microbiology*, **8**, 100−113.

Williams, T.M. and Owen, R.B. (1992) Geochemistry and origins of lacustrine ferromanganese nodules from the Malawi Rift, Central Africa. *Geochimica et Cosmochimica Acta*, **56**, 2703−2712.

Xu, H.F., Chen, T.H., and Konishi, H. (2010) HRTEM investigation of trilling todorokite and nano-phase Mn-oxides in manganese dendrites. *American Mineralogist*, **95**, 556−562.

Xu, H.F., Shen, Z.S., and Konishi, H. (2014) Si-magnetite nano-precipitates in silician magnetite from banded iron formation: Z-contrast imaging and ab initio study. *American Mineralogist*, **99**, 2196−2202.

Ying, X. and Axe, L. (2005) Synthesis and characterization of iron oxide-coated silica and its effect on metal adsorption. *Journal of Colloid and Interface Science*, **282**, 11−19.